Compressive transverse fracture behaviour of pultruded GFRP materials: experimental study and numerical calibration

Lourenço Almeida-Fernandes [1], Nuno Silvestre [2], João R. Correia [3], Mário Arruda [4]

[1] Phd Student, CERIS, Instituto Superior Técnico, Universidade de Lisboa, Portugal
(lourenco.a.fernandes@tecnico.ulisboa.pt)
[2] Full Professor, IDMEC, Instituto Superior Técnico, Universidade de Lisboa, Portugal
(nsilvestre@tecnico.ulisboa.pt)
[3] Full Professor, CERIS, Instituto Superior Técnico, Universidade de Lisboa, Portugal
(joao.ramoa.correia@tecnico.ulisboa.pt)
[4] Research Associate, CERIS, Instituto Superior Técnico, Universidade de Lisboa, Portugal
(mario.rui.arruda@tecnico.ulisboa.pt)

Abstract

This paper presents a study on the transverse fracture behaviour of pultruded glass fibre reinforced polymer (GFRP) materials in compression, namely the assessment of transverse compressive fracture toughness (G_2^-) and transverse compressive residual strength (σ_r). These properties were assessed through experimental Compact Compression (CC) tests of six different GFRP materials, which were coupled with a data reduction method to determine experimental predictions of G_2^- and numerically calibrated as a function of the experimental load *vs.* displacement curves. Through this process, the expected experimental overestimation of G_2^-, attributed to contact stresses behind the notch tip, was evaluated and accurate numerical estimates of G_2^- were determined. The numerical calibration considered both G_2^- and σ_r, by considering a bi-linear cohesive law. Through the numerical calibration, the G_2^- results ranged between 36 and 67 N/mm and σ_r values varied from 9% to 16% of transverse compressive strength (7.6 and 16.9 MPa, in absolute values). Finally, the G_2^- results were analysed as a function of transverse fibre reinforcement percentage and compared to transverse tensile fracture toughness results (G_2^+) determined in a previous work. This study showed that G_2^- is generally higher than G_2^+ and that the compressive-to-tensile ratio is inversely proportional to the transverse reinforcement percentage.
Keywords: A. Pultruded FRP composites; B. Fracture toughness; C. Damage mechanics; C. Notch.

1. Introduction

The compressive fracture properties of pultruded glass fibre reinforced polymer (GFRP) profiles are still very poorly characterized [1-5]. This stems from the complex damage propagation mechanisms that develop under compressive loads, which encompass fibre kinking, delamination, post-failure contact and their interaction. Research efforts have been put on studying these various failure modes and their relevance on compressive properties of GFRP materials [4, 5]. However, there is still very limited information on their compressive fracture properties. This absence constitutes a severe limitation to a reliable use of advanced computational simulations in assessing the strength of GFRP structures or components, thus hindering their widespread use in engineering design practice. For instance, the failure of beam-to-column connections [6] and web-crippling of beams [7-9] cannot be correctly predicted through currently available stress-based criteria. Often, the validation of these computational models requires a trial-and-error adoption of GFRP fracture properties to match the experimental ultimate strength of a given structure or component.

The transverse tensile fracture properties of composites have been extensively characterized, mostly carbon FRP (CFRP) laminates [3, 5, 10, 11] and, to some extent, pultruded GFRP materials [12-15]. Currently, a consistent basis for the assessment of fracture properties exists for tensile loading, but not for compressive loading. This discrepancy may be explained by two factors: (i) as mentioned, the compressive failure mode is more complex than the tensile one, comprising different damage mechanisms [3, 4]; and (ii) the inadequacy of tensile fracture toughness procedures and techniques

when applied to compression [2, 3]. This inadequacy results from the fact that tensile damage involves crack opening and separation of damaged fronts, while compressive damage involves crushing and continued contribution of the damaged fronts in contact, which lead to residual strength [2-4] and to an overestimation of fracture properties.

This paper presents a study on the transverse compressive fracture toughness (G_2^-), also known as critical energy release rate, and transverse compressive residual strength (σ_r) of pultruded GFRP materials. An experimental study was conducted, based on Compact Compression (CC) tests, which were coupled with data reduction methods to determine the experimental estimates of energy release rate throughout each test. As fracture tests were expected to overestimate the transverse compressive fracture toughness directly (through data reduction methods, due to contact stresses behind the notch tip), the load *vs*. displacement results were used in an inverse methodology to calibrate the relevant damage parameters and thus establish an estimate of the fracture properties [16, 17]. Therefore, the experimental load *vs*. displacement curves were fitted with numerical results, in order to determine numerical estimates of G_2^-. The aforementioned contact stresses were also taken into account in the calibration of the numerical models, by considering a residual stress for transverse compression. A bilinear cohesive law [18] with an initial softening stage (beyond the maximum load) was adopted, followed by a constant σ_r plateau. Therefore, two main parameters were considered in the numerical calibration procedure: (i) G_2^- and (ii) σ_r. These parameters were calibrated for six different pultruded GFRP materials in order to obtain the best fit between experimental and numerical load *vs*. displacement curves and to investigate the influence of varying the fibre reinforcement in those parameters. To this end a user defined material (UMAT) subroutine was developed within the framework of Abaqus software [19].

2. Experimental study

2.1. Materials

The present study addressed a total of six polyester based pultruded GFRP materials that have been previously studied in regard to their transverse tensile fracture toughness [14, 15]. The pultruded GFRP materials were taken from: I-sections of Fiberline Composites (FC), Creative Pultrusions (CP), Alto Perfis Pultrudidos (AP) and STEP (ST), a plate from AP and a U-section from ST. The material was labelled as follows: (i) section geometry, "I"-section, "U"-section or pultruded plate (P); (ii) profile height or plate width; and (iii) supplier initials. In the experimental program presented ahead, each material was tested through a minimum of four specimens using standard experimental procedures [14,15]. The material mechanical properties are summarized in Table 1, including longitudinal (1) and transverse (2) properties, for tensile (+) and compressive (-) loading. The properties of profile I150-AP obtained earlier [15] have been updated based on new material characterization tests (Table 1), due to concerns about the potential influence of production defects (low fibre-matrix bond) found in a previous batch, as discussed in [15].

Table 1: Average geometric and mechanical properties of the various pultruded GFRP materials.

Material	Ref.	Height / Width [mm]	Wall thick., t [mm]	Layup	Trans. Reinf. %*	E_{11}^- (GPa)	E_{22}^+ (GPa)	E_{22}^- (GPa)	G_{12} (GPa)	σ_{u11}^+ (MPa)	σ_{u22}^+ (MPa)	σ_{u22}^- (MPa)	τ_{u12} (MPa)
I200-FC	[14]	200x 100	9.9	W [0/90]	8.3	29.9	11.9	10.8	2.9	323	71	122	67
I150-AP		150x 75	8.1	W [0/90]	4.5	44.0	9.6**	7.8	3.1	384	45**	60	48
P300-AP		300x 5.3	5.3	W [0/90]	12.3	33.6	12.2	15.1	5.4	258	71	135	82
I152-CP	[15]	152x 76	6.3	Q	29.7	24.6	10.3	10.9	4.0	416	121	104	65
I150-ST		150x 75	8.1	CFM	0.0	28.1	5.5	9.3	3.2	377	34	123	70
U150-ST		150x 45	7.7	Q	20.0	25.8	5.8	6.5	4.2	353	69	84	71

* considering 90° and 45° (multiplied by $\sqrt{2}/2$) oriented layers; CFM layers were disregarded.

** updated from [15], based on more recent tests.

These GFRP materials can be divided in respect to their transverse reinforcements into three main fibre layup categories: (i) unidirectional layups where the transverse reinforcements are made of continuous filament mats (CFM), with randomly oriented fibres, which provide a low reinforcing effect in all directions; (ii) cross-ply materials, transversely reinforced through woven layers with fibres oriented at 0° and 90° in respect to the roving direction (W[0/90]); and (iii) quasi-isotropic layups, reinforced through ±45° and 90° oriented layers (Q). These layups are also identified in Table 1, leading to different percentages of transverse reinforcement. These percentages were based on calcination tests (procedure detailed in [15]), considering only 90° and 45° (multiplied by $\sqrt{2}/2$) oriented layers.

The material properties reported for the transverse direction were based on compressive coupon tests. These tests were conducted using a combined load in compression (CLC) test setup, following the specifications of the ASTM D6641M – 09 standard [20]. Exceptionally, the length of some specimens (oriented perpendicularly to the profile/pultrusion axis) did not fulfil those specifications due to the limited web height of the profiles. In these instances (I150-AP, I152-CP, I150-ST and U150-ST), the specimen nominal length was 120 mm.

2.2. Specimen geometries

After preliminary tests conducted on both (i) CC specimens with 60 mm of width and (ii) Wide Compact Compression (WCC) specimens with 120 mm of width, several unintended failure modes were detected and thus, a scaled-up CC specimen geometry was implemented with a nominal width of 120 mm. This geometry, detailed in Figure 1, contributed to reduce the shear-out failure at the loading holes and enabled the development of significant damage propagation lengths. Given these results, this scaled-up geometry was adopted for all materials. In general, a total of 6 specimens were tested for each material.
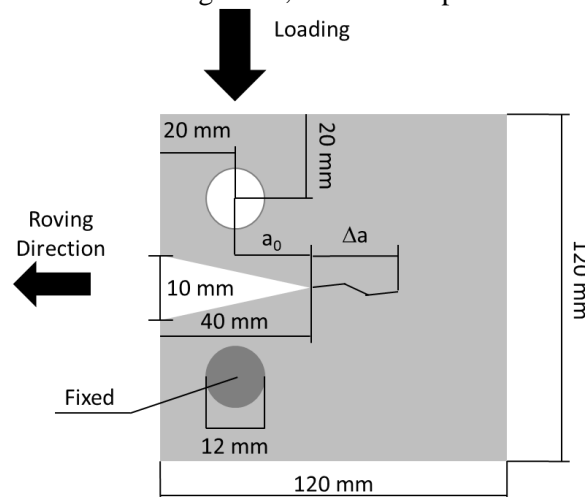

Figure 1: Scaled-up CC test geometry.

2.3. Test setup

The specimens were painted with white matte paint and targets were inserted for photogrammetry, using a black marker pen. A video-extensometer equipment (Sony camera, model XCG 5005E with Fujinon lens) with a resolution of 5 MP, a data acquisition rate of 10 Hz and an image acquisition of 1 FPS was used to monitor these targets. This methodology was implemented to monitor the crack mouth closing displacement (CMCD), the crack tip closing displacement (CTCD) and damage propagation (Δa). This last parameter was also monitored through a digital microscope, (Dino-Lite Edge Digital USB Microscope, model AM7915MZT) with a resolution of 5 MP and a maximum frame rate of 30 FPS, facing the posterior face of the specimen. The experimental tests were conducted at a displacement rate of 1.0 mm/min and the measurements are schematically illustrated in Figure 2.

2.4. Data reduction

Following previous studies conducted on tensile fracture tests [14, 15, 21, 22], the finite element based J-integral method was implemented. This method consists of developing a series of numerical models

with increasing pre-defined (imposed) damage lengths and having a unit load (1 N) applied. The energy release rate measured in these models is then computed as a function of damage propagation length and experimental applied load [3, 10, 14]. These numerical models are similar to those reported in earlier works [14, 15], having S4R shell elements and an average mesh size of 0.5 mm. The boundary conditions were applied to the loading holes through a "Coupling" constraint. The J-integral estimates for each damage propagation increment were determined through the "Crack" tool, propagated to each new length by using the "Seam" tool. This methodology has been widely validated for tensile fracture tests [3, 10], but has been deemed unsuitable for compressive fracture tests [2, 3] as it neglects the aforementioned contact stresses behind the notch tip that lead to overestimations of G_2^-. Therefore, the experimentally determined energy release rate results presented in the following section should be taken as overestimations of G_2^-. This trend will be further established by comparing such J-integral based predictions of G_2^- to the numerically calibrated results presented in section 4.
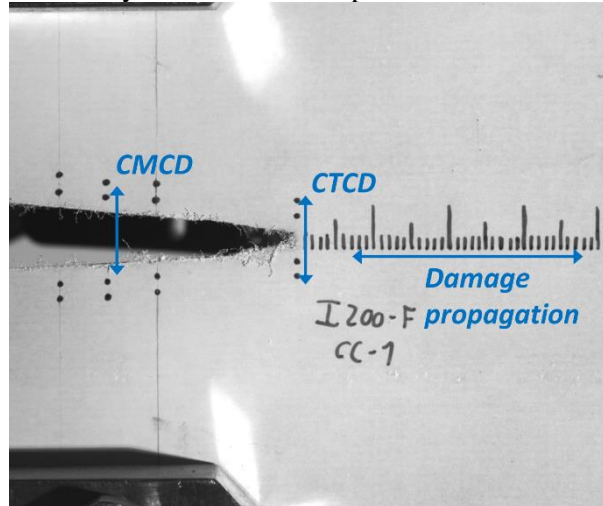

Figure 2: Measurements taken from CC tests.

It should be highlighted that these models are perfectly elastic and they do not aim to simulate the fracture tests, but only the variation of the J-integral estimates for different pre-defined (imposed) damage propagation lengths. In order to simulate the fracture tests, a non-linear damage formulation is required, as detailed in section 3.

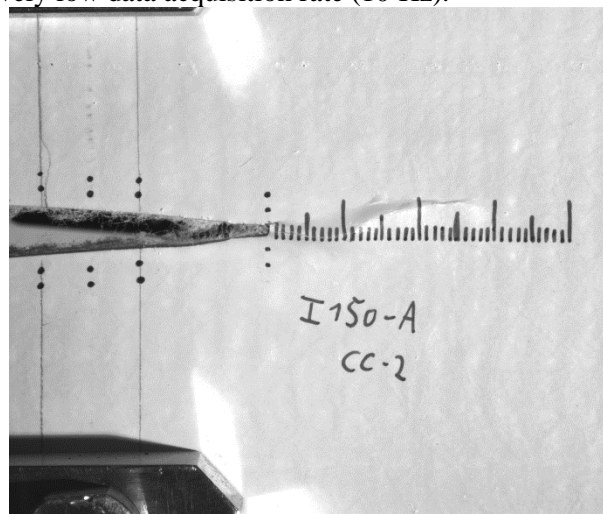## 2.5. Experimental results

2.5.1. Failure modes

Due to compressive stresses, all specimens showed initial damage at the notch tip, which propagated in the shape of a kink band associated with interlayer delamination (separation of layers). After some damage propagation that varied quantitatively across different materials, two main failure modes were reported: (i) buckling failure during the softening stage, which occurred at a stable rate; and (ii) failure due to transverse tensile stresses at the posterior face of the specimen, which was brittle. Figure 3 presents an example of compressive damage growth (kink band), buckling failure and tensile failure. The specimens P300-AP, I152-CP and U150-ST presented predominantly buckling failure, while specimens I200-FC, I150-AP and I150-ST exhibited clear signs of tensile failure. Regarding the data reduction process, all measurements were stopped as soon as one of these failure modes was noticeable. Note that tensile failure occurred in those specimens with lowest ultimate transverse tensile stresses (I150-AP and I150-ST) and highest thickness (I200-FC). The other specimens showed evidence of out-of-plane bending during the softening stage, after significant damage propagation had developed.
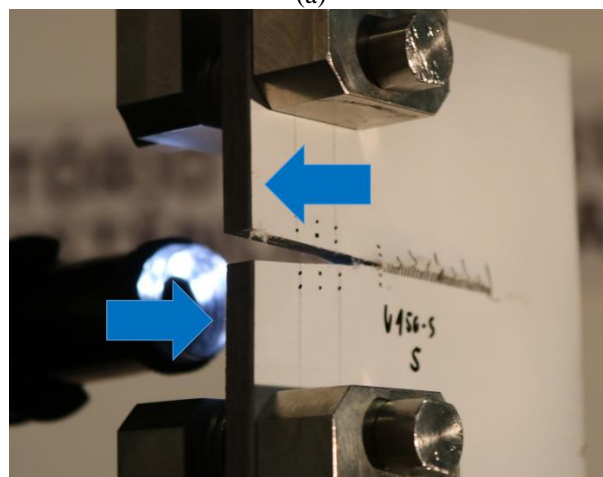
2.5.2. Load vs. CMCD curves

Figure 4 presents a summary of load vs. CMCD curves, including experimental observations of tensile damage initiation. A similar trend can be found across all materials (except one): initial linear path to the peak (ultimate) load, followed by a nonlinear descending branch and a final softening stage. The exception was I200-FC, which showed a slight load drop after the linear path and then recovered in a

non-linear trend up to the peak load. This behavioural aspect was attributed to delamination, a phenomenon that is more relevant in thicker materials, such as I200-FC (9.9 mm).

Figure 4 also highlights a significant variability across different materials, which is in line with the geometry and material properties reported in Table 1. This variability is highlighted in the average ultimate load results, which vary from 7.5 kN (P300-AP) to 13.0 kN (I200-FC), as well as in the softening stages of different materials. It is noticeable that there is a high consistency in stiffness and ultimate load for each material, the exception being I150-ST (in this case, two specimens presented larger initial notch lengths and thus presented lower stiffness and ultimate load). The softening slopes ahead of the ultimate load also seem to be consistent across most specimens of a given material, which is a relevant remark regarding the potential calibration of numerical models. In this regard, the I150-AP and I150-ST specimens were discarded because tensile failure occurred too early and prevented the development of relevant compressive damage lengths. This trend can be observed in Figures 4 (b) and (e), where tensile damage initiation occurs in the beginning of the softening stage. Furthermore, Figure 4 (e) presents sudden load drops caused by tensile damage in I150-ST load *vs*. CMCD curves. Some load drops led to odd readings of data (illustrated in Figure 4 (e)), due to the brittle nature of failure and possibly due to the relatively low data acquisition rate (10 Hz).
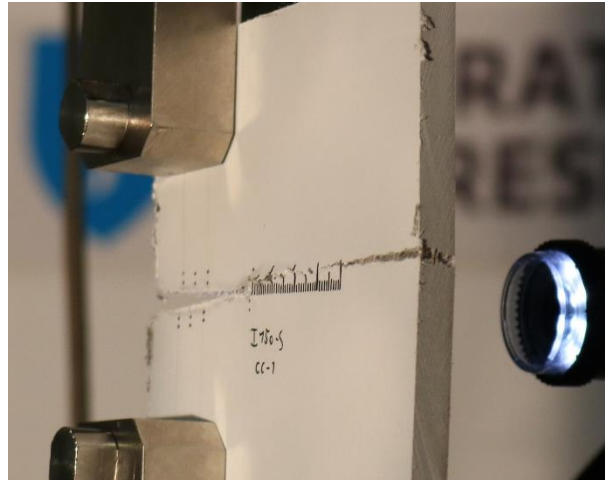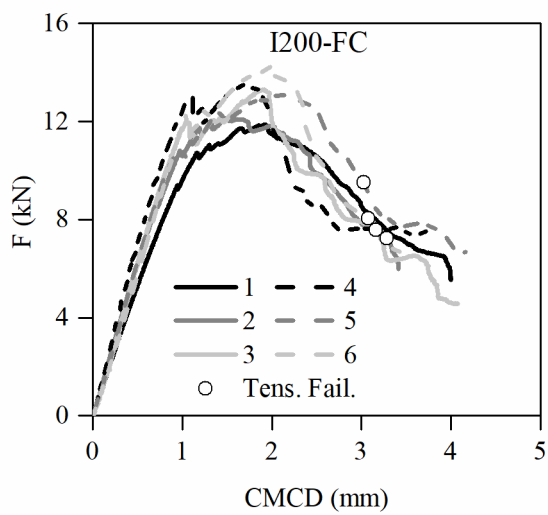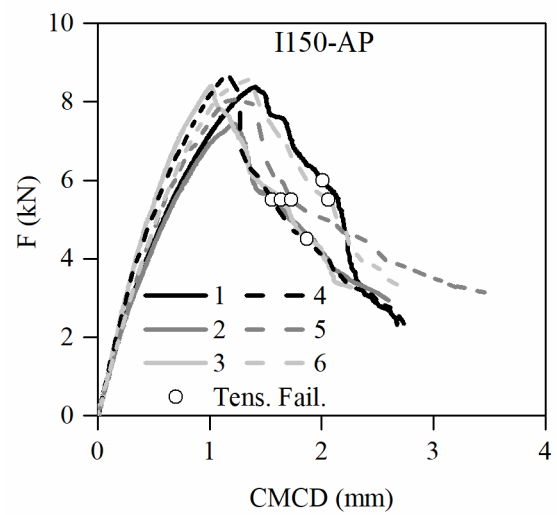
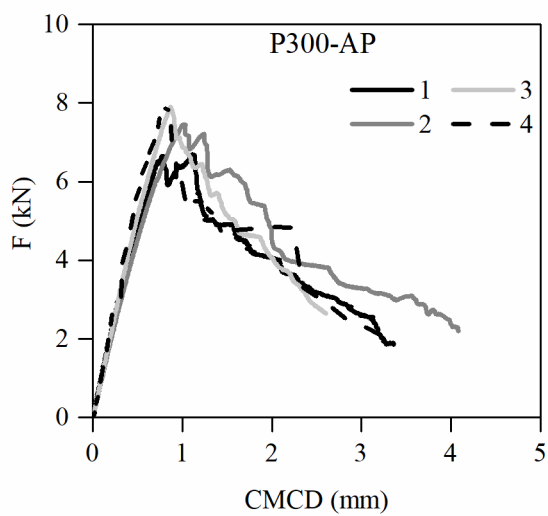

(a)

(b)

(c)

Figure 3: CC test failure modes: (a) compressive damage propagation; (b) buckling failure; (c) tensile failure.
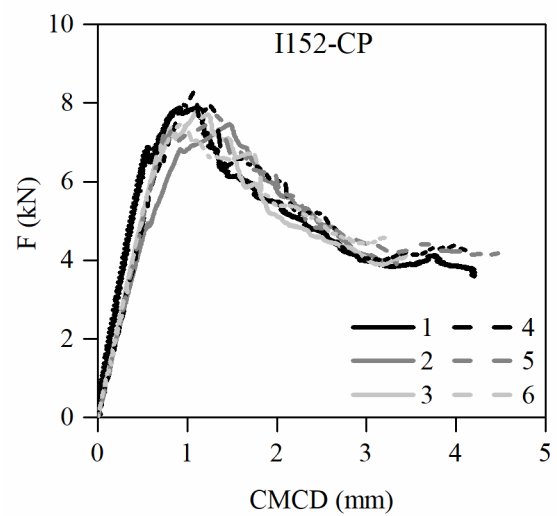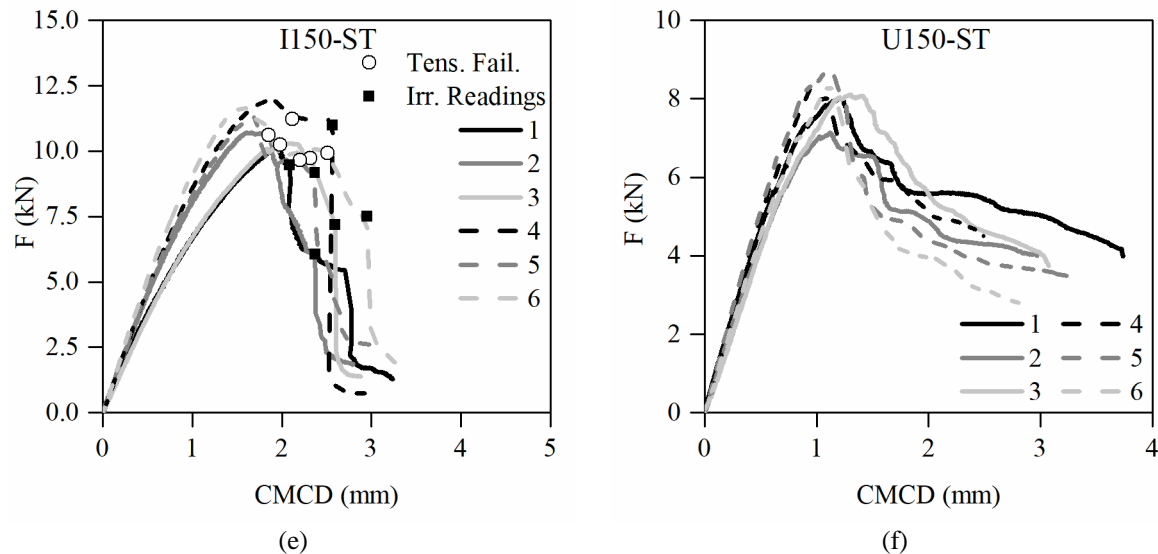

(a)

(b)

(c)

(d)

Figure 4: Experimental CC load *vs*. CMCD curves: (a) I200-FC; (b) I150-AP; (c) P300-AP; (d) I152-CP; (e) I150-ST; (f) U150-ST.

2.5.3. Fracture toughness results

Figure 5 presents energy release rate (G) *vs*. CTCD curves for each material. It is noticeable that all materials presented a significant scatter among the various specimens. This scatter was attributed to the complexity of the damage propagation process and to the delamination near the notch tip (kink band), which hindered an accurate and objective measurement of damage propagation. The high scatter, aside from the issue of contact between notch faces, invalidated potential measurements of an initial cohesive stress that could be compared to the material strength, similarly to what was done in previous studies on tensile fracture tests [14, 15].

3. Numerical study

3.1. Geometry and boundary conditions

The geometry adopted for the modelled specimens is that displayed in Figure 1. The initial notch length (a_0) matched the average value measured for each material, instead of the nominal value of 40 mm. Initially, the semi-circular notch tip with a radius of 2 mm was inserted, like that of test specimens (Figures 6 (a)-(b)). However, preliminary simulations showed that the severe distortion caused to the element mesh surrounding the notch tip led to earlier onsets of damage propagation and, therefore, to lower ultimate loads. Alternatively, a triangular notch tip was implemented, as illustrated in Figure 6 (c), which led to a more uniform element mesh and thus to higher ultimate loads.

The boundary conditions were applied at the loading holes (see Figure 1). The centre of each loading hole was connected to the relevant half-circumference through the "Coupling" tool, in order to mimic the experimental test. One loading hole was restrained in terms of horizontal and vertical displacements, whereas the other was restrained horizontally and had an imposed vertical displacement. The imposed displacements followed the CMCD monitored for each experimental series. Because the out-of-plane buckling is a phenomenon intrinsic of the test and does not play a role at the material characterization level, it was not simulated.
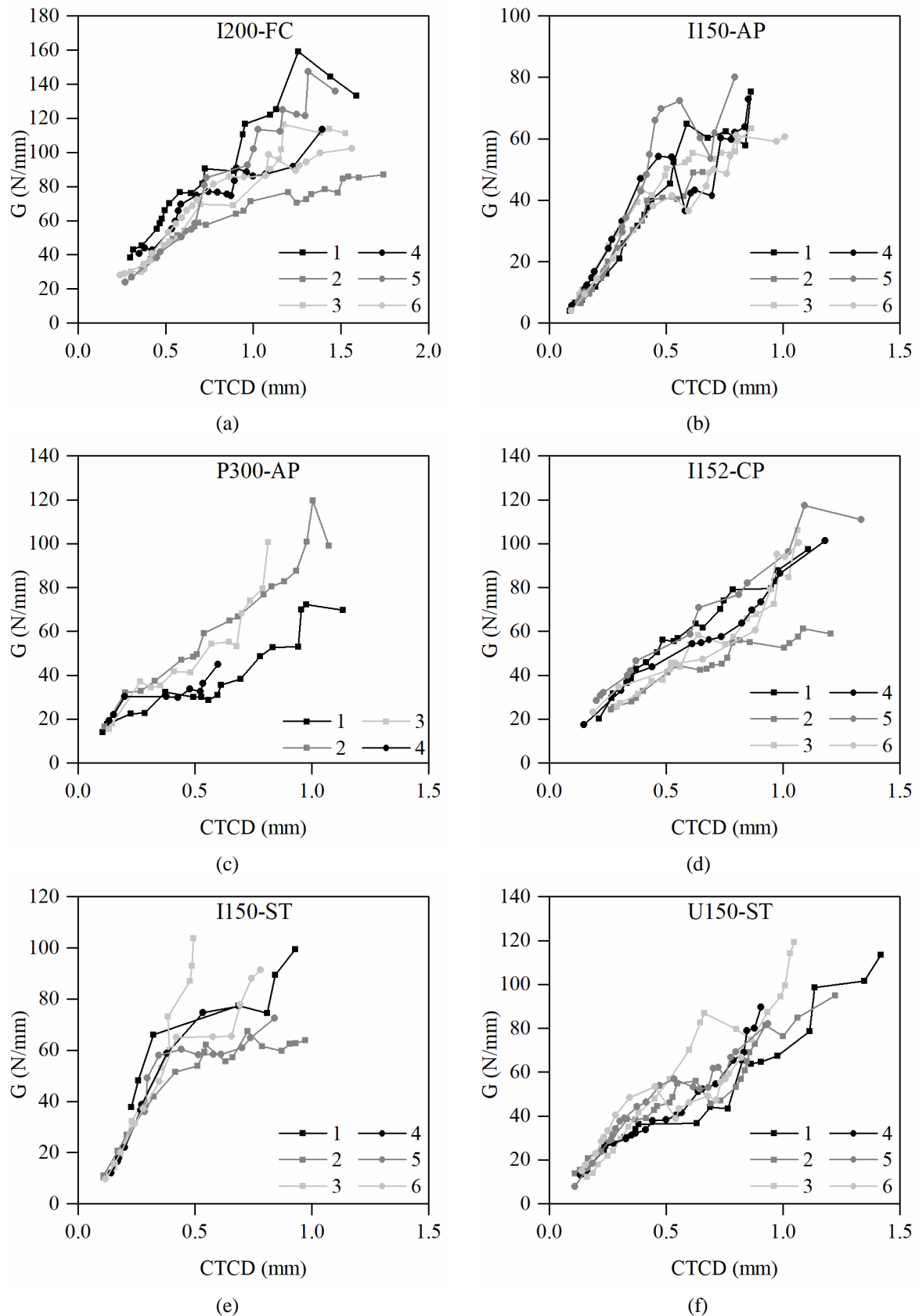
Figure 5: FE J-integral based G *vs*. CTCD curves: (a) I200-FC; (b) I150-AP; (c) P300-AP; (d) I152-CP; (e) I150-ST; (f) U150-ST.
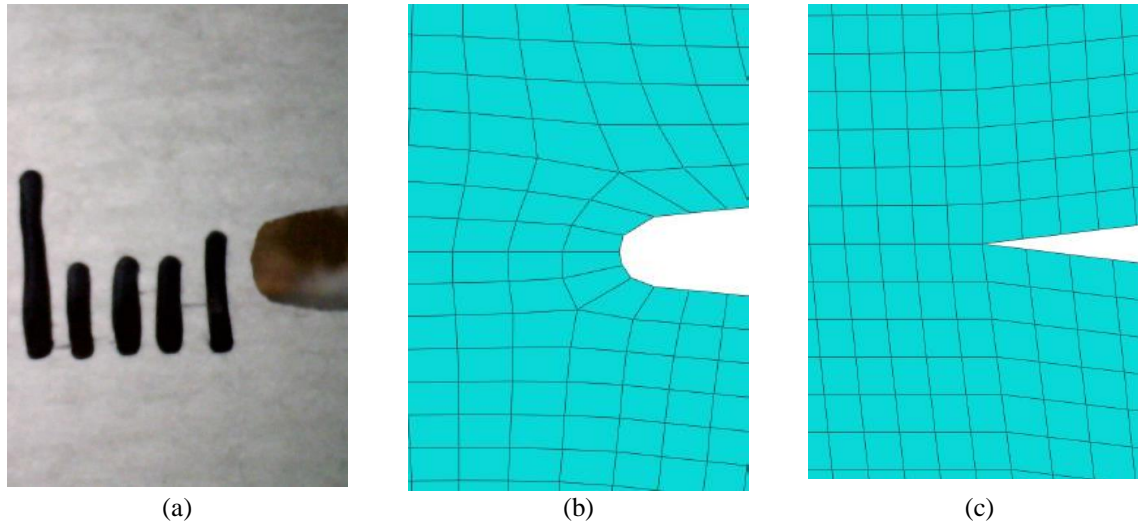
(a)   (b)   (c)

Figure 6: Initial notch tip shapes: (a) I200-FC-1 specimen; (b) numerical model with round notch; (c) numerical model with triangular notch.

3.2. Material properties and damage

The material properties implemented in the numerical models are those reported in Table 1, considering the compressive elastic modulus for the transverse direction (E_{22}^-). Regarding fracture properties, the longitudinal fracture toughness parameters (G_1^+ and G_1^-) were set to 100 N/mm [23] and should have no influence on the results (no test showed signs of damage propagation in the longitudinal direction). The transverse tensile fracture toughness (G_2^+) was defined in accordance to previous studies [14, 15] (Table 2). These values are particularly relevant in case of tensile failure modes (I200-FC, I150-AP and I150-ST). The cohesive stresses (σ_c) for transverse tensile loading, determined by assessing the G *vs*. crack tip opening displacement (CTOD) initial slopes [14, 15], are also displayed in Table 2. As mentioned, the properties of I150-AP presented in Table 2 were updated from [15], by considering new material characterisation tests (*cf*. Table 1). It is noteworthy that I150-AP is the only material to present $\sigma_c < \sigma_{u22}^+$.

The transverse compressive fracture toughness (labelled as G_2^-) was calibrated as a function of the experimental ultimate loads, considering a range from 0 to 70 N/mm. Finally, the residual stress that results from the contact between notch faces was calibrated for the fitted G_2^- results, as a function of the experimental softening slopes.

Damage initiation was determined through the Hashin criterion [24]. Damage evolution was implemented through a UMAT subroutine, so that the typical linear law implemented in Abaqus [19] could be modified. A bilinear cohesive law based on previous studies [17, 18] was implemented, as illustrated in Figure 7. The following customized cohesive law (Figure 7) was defined:

Table 2: Experimental transverse tensile fracture toughness and cohesive stress results [14, 15].

Material	I200-FC	I150-AP	P300-AP	I152-CP	I150-ST	U150-ST
G_2^+ (N/mm)	20.2 ± 2.5	13.6 ± 2.2*	21.3 ± 3.0	160.0**	9.9 ± 0.9	25.8 ± 3.1
σ_c (MPa)	80	32*	132	184	41	86

* properties revised in accordance to the updated mechanical properties presented in Table 1.

** as a stable propagation stage was not reached, this value was considered as a conservative estimate.

-    Descending path:

$$\sigma_r = x\sigma_{eq}^0; \quad 0 \leq x \leq 1; \quad k_r = (1-d_r)k_{eq} \quad k_{eq} = \frac{\sigma_{eq}^0}{\delta_{eq}^0} \tag{1}$$

-    Point A:

$$\begin{cases} \sigma_r = (1 - d_A)k_{eq}\delta_{eq}^A = (1 - d_A)\dfrac{\delta_{eq}^A}{\delta_{eq}^0}\sigma_{eq}^0 = x\sigma_{eq}^0 \\[2mm] (1 - d_A) = \dfrac{\delta_{eq}^0(\delta_{eq}^u - \delta_{eq}^A)}{\delta_{eq}^A(\delta_{eq}^u - \delta_{eq}^0)} \end{cases} \Rightarrow \delta_{eq}^A = \delta_{eq}^u - x(\delta_{eq}^u - \delta_{eq}^0) \tag{2}$$

- Residual stress plateau:

$$\sigma_{eq} = (1 - d_r)k_{eq}\delta_{eq} = \sigma_r = x\sigma_{eq}^0$$

$$\Leftrightarrow (1 - d_r)\frac{\sigma_{eq}^0}{\delta_{eq}^0}\delta_{eq} = x\sigma_{eq}^0 \tag{3}$$

$$\Leftrightarrow d_r = 1 - x\frac{\delta_{eq}^0}{\delta_{eq}}$$

where σ_r is the implemented residual stress, σ_{eq}^0 is the material ultimate stress, x is the ratio of σ_r/σ_{eq}^0, k_r is the stiffness at the residual stress plateau, d_r denotes the damage variable for the residual stress plateau, k_{eq} is the undamaged stiffness, δ_{eq}^0 is the displacement for the ultimate or cohesive stress, δ_{eq}^u is the displacement for zero stresses, if no residual stress was considered. Other than the customized cohesive law, the damage initiation and evolution expressions are similar to those implemented in Abaqus [19], as detailed in [21].
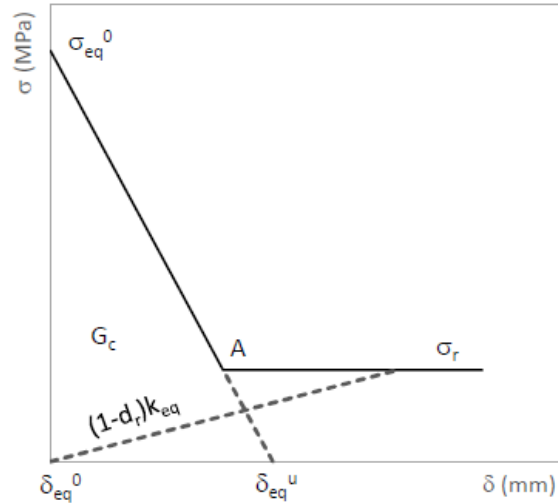

Figure 7: Bilinear cohesive law, with residual stress (σ_r).

3.3. Finite element mesh

CPS4 finite elements were used because both specimen geometry and loading are in-plane. CPS4 are bi-linear plane stress four node quadrilateral elements, with full integration (4 gauss points) and three degrees-of-freedom per node. A parametric study was performed to establish the sensitivity of the results to the mesh average size. Models having meshes with 0.25, 0.5, 1.0 and 2.0 mm finite element sizes were considered for the I152-CP material. In this instance, G_2^- was considered as 40 N/mm, corresponding to 25% of G_2^+ (160 N/mm). The residual stress was set to 20% (20.8 MPa) of the transverse compressive strength (σ_{u22}). Figure 8 presents load vs. CMCD curves for the I152-CP material obtained from the numerical models with different meshes.
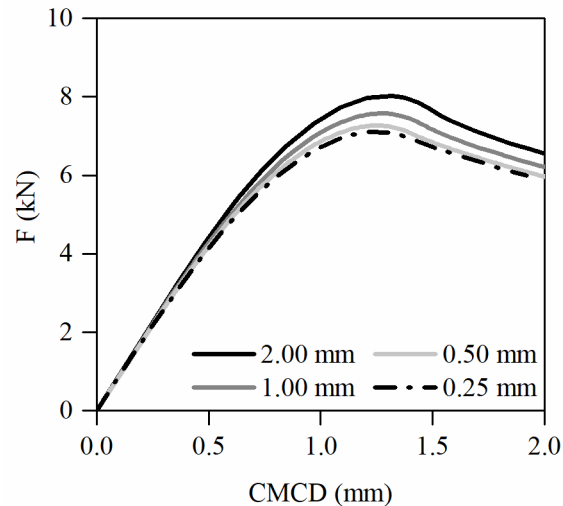
Figure 8: Numerical load *vs.* CMCD curves of I152-CP material.

Figure 8 shows that there is a low sensitivity to the mesh size, as the ultimate loads appear to stabilize for 0.25 and 0.5 mm mesh sizes. These models led to significant differences regarding the number of elements for each element size, as summarized in Table 3. The number of elements for meshes with 0.5 mm, 1.0 mm and 2.0 mm sizes was respectively 25%, 6.3% and 1.6% of the mesh with 0.25 mm size.

Table 3: Characterization of I152-CP FE mesh for different average FE sizes.

Finite element average size	Number of elements	Degrees of Freedom	Total CPU time (s)*	Ultimate load
2 mm	3362	7038	232	8.03
1 mm	13527	27672	3171	7.58
0.5 mm	54240	109718	18564	7.27
0.25 mm	215325	433124	123060	7.12

* All models ran in 3 parallel processors in an Intel(R) Core(TM) i7-6700K CPU @ 4.00 GHz, with 64 GB of RAM.

The 2.0 mm mesh produced an ultimate load with a relative difference of 10.5% to the 0.5 mm mesh, whereas the 1 mm mesh provided an ultimate load with a relative difference of 4.2% in comparison to the 0.5 mm mesh. As computational time is also a relevant issue, the 1.0 mm mesh was selected to run the significant number of models detailed in the following sections, as it presents a reduced relative difference to more refined models, in terms of ultimate load ($\approx$4%), and also a moderate computational time. More details on mesh refinement of finite element models for damage of composite materials can be found in [21, 22].

4. Calibration of damage evolution parameters

The calibration of damage evolution parameters was conducted through a three-step procedure: (i) first, a preliminary calibration of G_2^- was made, as a function of the experimental ultimate loads (F_u, section 4.1); (ii) next, the G_2^- results were recalibrated as a function of experimental load *vs.* CMCD curves, and the transverse tensile ultimate stress (σ_{u22}^+) was also assessed, by considering either the material strength (Table 1) or the cohesive stress (σ_c, Table 2), being validated as a function of experimental observations of tensile damage at the posterior face of the specimen (section 4.2); and, (iii) finally, the residual stresses (σ_r) were calibrated based on the softening slopes of those curves obtained from tests (section 4.3). These analysis steps are illustrated in Figure 9. Additionally, for one profile (I150-ST), the potential effect of the relative difference between the transverse compressive and tensile elastic moduli (9.3 vs. 5.5 GPa) on numerical predictions of tensile failure was assessed. This analysis was included in step (ii).
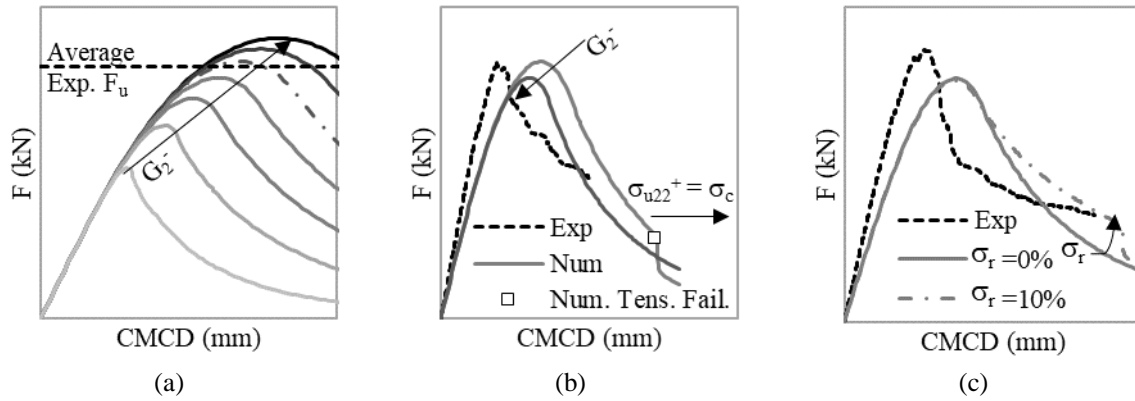
Figure 9: Numerical analysis steps: (a) calibration of G_2^- with average experimental ultimate loads; (b) calibration of G_2^- and assessment of σ_{u22}^+ based on experimental load *vs.* CMCD curves and failure modes; (c) calibration of σ_r with experimental softening slopes.

4.1. Ultimate loads

In the preliminary calibration of G_2^- a range between 10 and 70 N/mm was defined and, in this first stage, no residual stress was considered ($\sigma_r=0$). Figure 10 shows load *vs.* CMCD curves for I152-CP and U150-ST materials, enabling a comparison between the numerical curves with different G_2^- values and the experimental ones.
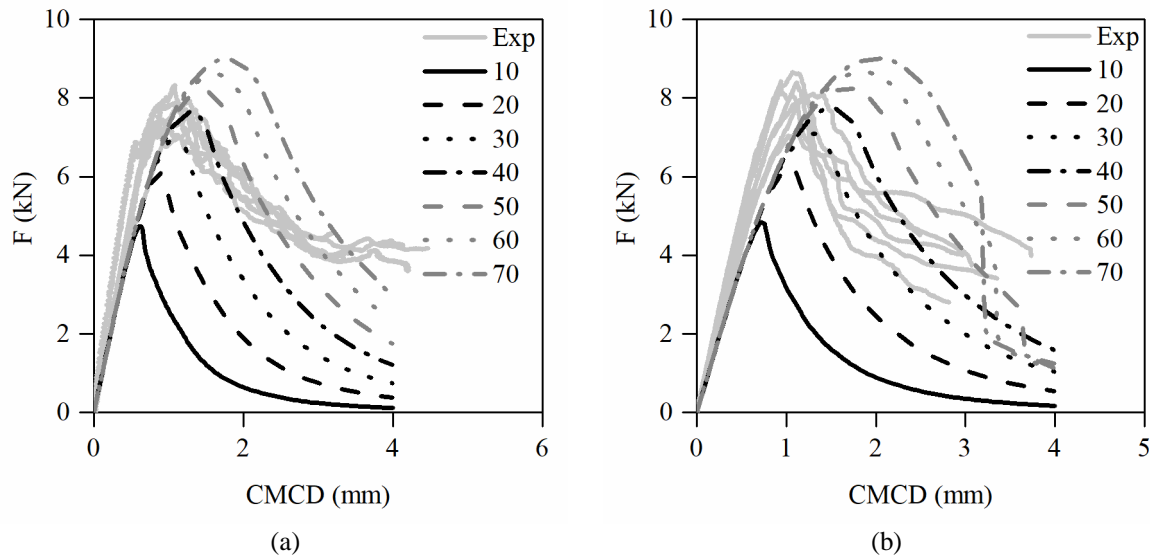

Figure 10: Numerical and experimental load *vs.* CMCD curves, considering input values of G_2^- (N/mm): (a) I152-CP; (b) U150-ST.

Figure 10 illustrates two different scenarios: (i) the curve peak and its initial softening path for the I152-CP model with G_2^- = 40 N/mm agrees fairly well with the experimental counterparts (Figure 10 (a)); (ii) the U150-ST models seem to be unable to reproduce correctly the experimental counterparts (Figure 10 (b)). This is particularly noticeable for the numerical curve with G_2^- = 50 N/mm (Figure 10 (b)), which reaches an ultimate load similar to that of the experimental tests, but presents a significantly smoother softening path. Figure 11 presents the variation, with G_2^-, of the percentage relative difference between the numerical ($F_{u,num}$) and experimental ($F_{u,exp}$) ultimate loads for all materials.

Figure 11 illustrates two distinct trends: (i) the models I200-FC, P300-AP, I152-CP and U150-ST show the best fit to experimental results when calibrated with G_2^- values between 35 and 50 N/mm; (ii) the models I150-AP and I150-ST seem to tend asymptotically to the experimental results – note that increasing G_2^- progressively leads to lower increments of ultimate load. This last trend is related to the tensile failure in the models, which develops similarly to experimental tests, in the posterior face of the

specimen (see Figure 3). This interaction was expected for these materials as they presented tensile failure modes and the lowest ultimate transverse tensile stresses (see Table 1). Therefore, an additional analysis was conducted for I150-AP and I150-ST with increased tensile properties (σ_{u22}^+=200 MPa and G_2^+=100 N/mm), in order to better establish the influence of tensile failure on the results previously presented in Figure 11. These new results are presented in Figure 12, where models with no tensile failure are labelled "NT".
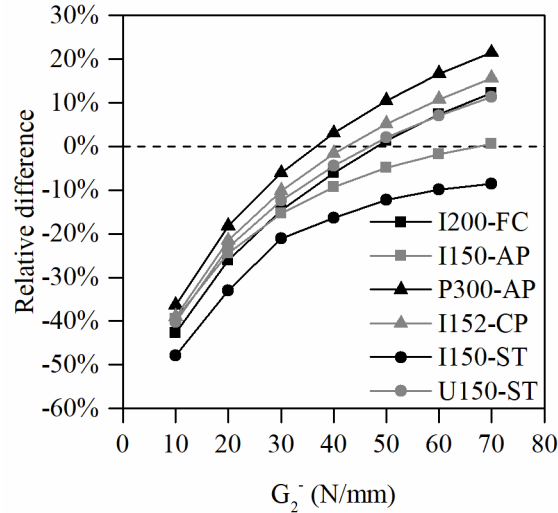

Figure 11: Variation, with G_2^-, of the percentage relative difference between the numerical ($F_{u,num}$) and experimental ($F_{u,exp}$) ultimate loads for all materials.

Figure 12 shows a significant difference in the results for I150-ST by disregarding the effect of tensile failure, while the results for I150-AP are less affected. Through this methodology, updated values for G_2^- were determined for I150-AP and I150-ST materials. Estimates of G_2^- that minimize the difference between numerical and experimental ultimate loads are summarized in Table 4.
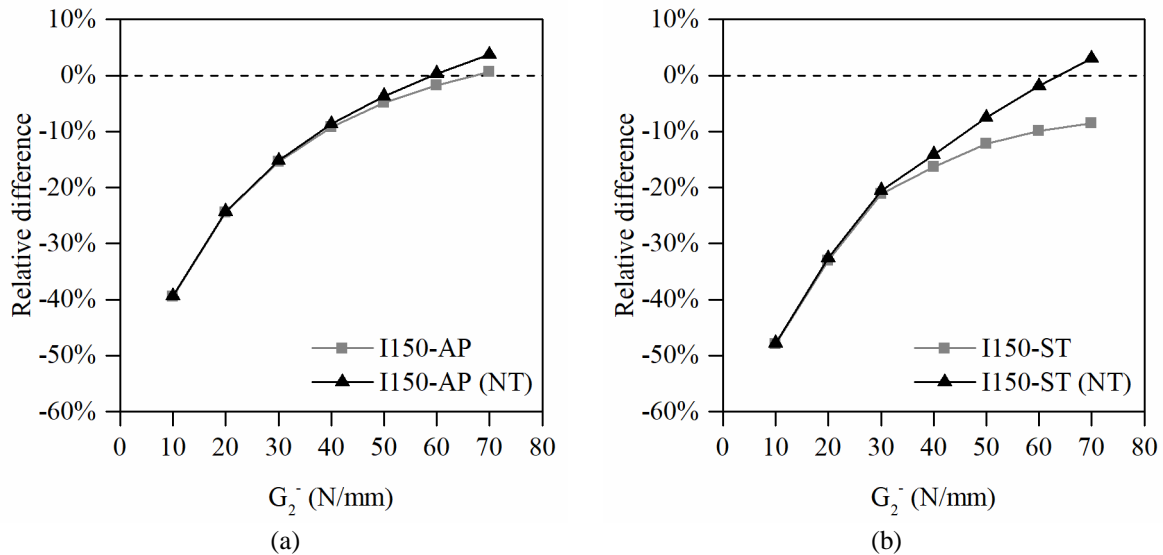

| (a) | (b) |

Figure 12: Variation, with G_2^-, of the percentage relative difference between the numerical ($F_{u,num}$)and experimental ($F_{u,exp}$) ultimate loads, disregarding tensile failure: (a) I150-AP; (b) I150-ST.

As expected, and due to the aforementioned reasons, the results summarized in Table 4 are significantly lower than the experimental ones presented in Figure 5 (experimental G_2^- > 100 N/mm for most materials). A fracture toughness range between ≈35 N/mm and ≈70 N/mm was determined for the pultruded GFRP materials tested under compression. These values are significantly higher than the typical values of G_2^+ (*cf.* Table 2), except for I152-CP.

Table 4: G_2^- values calibrated based on experimental average ultimate loads (N/mm).

| Material	I200-FC	I150-AP	P300-AP	I152-CP	I150-ST	U150-ST
G_2^-	48	59	36	42	67	47

4.2. Load *vs.* CMCD curves

4.2.1. Preliminary results

In this second stage, the previously determined G_2^- values and null residual stress (σ_r) were implemented in the numerical models. Figure 13 presents the load *vs.* CMCD curves for all tested materials, obtained from numerical analyses (with and without consideration of tensile failure, respectively "Num" and "Num NT") and from experimental tests ("Exp"). The experimental observations of tensile damage initiation were cross marked in the experimental load *vs.* CMCD curves of Figures 13 (a), (b) and (e) ("ETF"). Finally, the numerical tensile failure ("NTF") was also included for the numerical results.
The preliminary results reported in Figure 13 show some different trends. Firstly, most numerical results agree well with experimental ones in terms of stiffness – the exceptions are the I150-AP and U150-ST models, which presented slightly lower stiffness compared to tests. Secondly, experimental and numerical results of both P300-AP and I152-CP match reasonably well (Figures 13 (c) and (d)), moreover as the fitting between numerical and experimental softening slopes is expected to improve by considering $\sigma_r > 0$. Thirdly, the numerical models correctly predict tensile failure for I200-FC, I150-AP and I150-ST, however providing excessively conservative estimates of CMCD for the tensile failure of I200-FC and I150-ST (Figures 13 (a) and (e)). Additionally, the models conservatively predict the occurrence of tensile failure for P300-AP (Figure 13 (c)), at a CMCD level where experimental tests showed no evidence of tensile failure. Finally, it should be noted that both I150-AP and U150-ST tests were poorly simulated by the numerical models, as the numerical load *vs.* CMCD curves present a significantly smoother softening trend in the post-peak zone, when compared to experimental curves.

4.2.2. Calibration

Considering the results illustrated in Figure 13, where some materials presented excessively conservative predictions of tensile failure (Figures 13 (a), (c) and (e)), the cohesive stress (see Table 2) was thus considered instead of the transverse tensile material strength. This increase of material transverse tensile strength should contribute to a better fit between numerical and experimental predictions of ultimate failure for the I200-FC, P300-AP and I150-ST series. In a different trend, the lower cohesive stress of the I150-AP material leads to numerical tensile failure at lower CMCD levels; however, numerical results are in good agreement with documented experimental tensile damage initiation (*cf.* Figure 14 (b)).
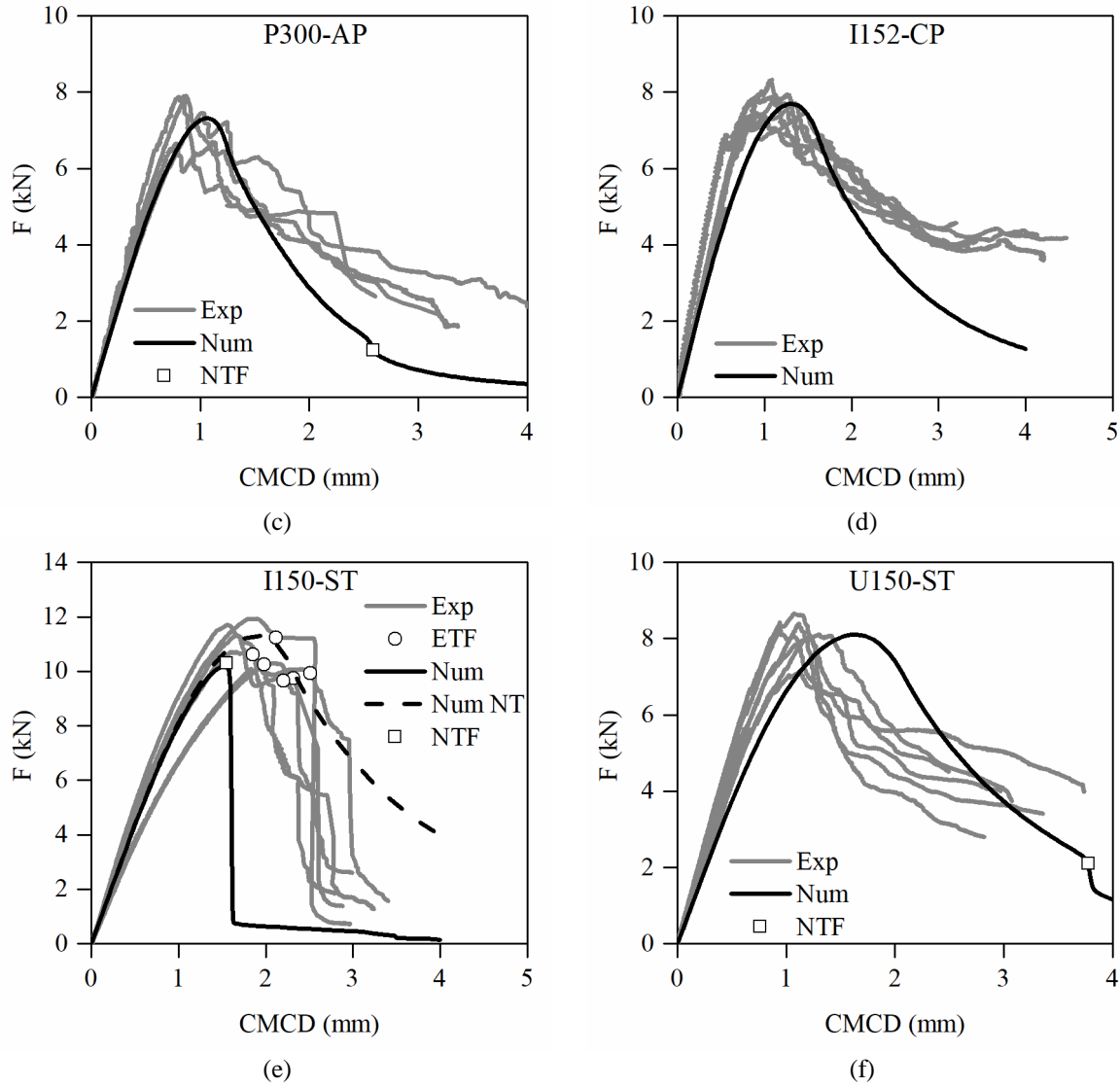

(a)

(b)
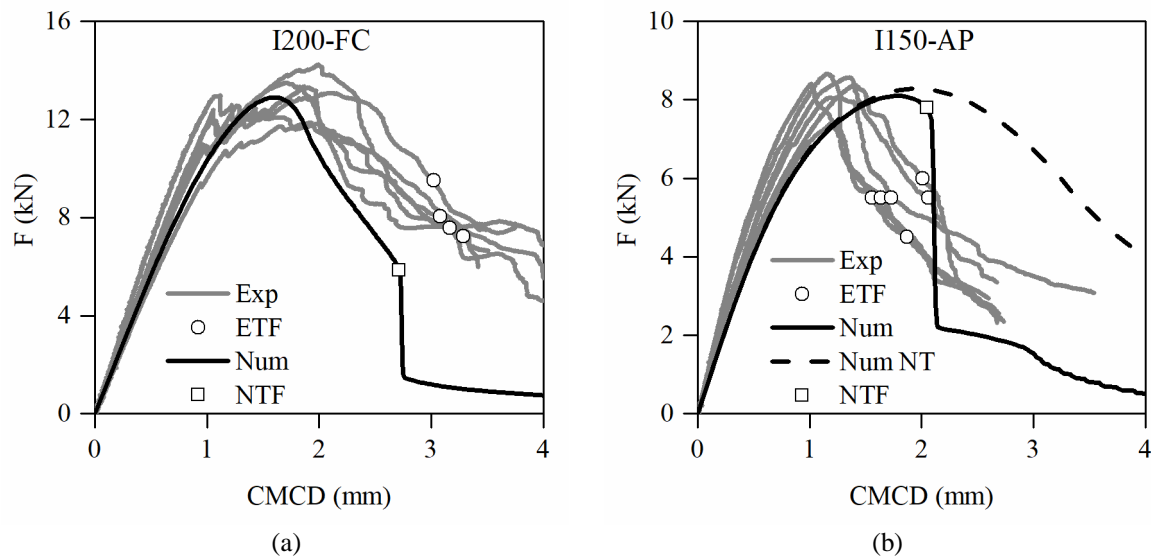
Figure 13: Experimental and numerical load *vs.* CMCD curves:
(a) I200-FC; (b) I150-AP; (c) P300-AP; (d) I152-CP; (e) I150-ST; (f) U150-ST.

For I150-AP and U150-ST materials (Figures 13 (b) and (f)), the significantly smoother numerical softening stage seems to indicate that the G_2^- may have been overestimated. This overestimation may indicate that the σ_{u22}^- properties considered for these materials may have been experimentally underestimated. Therefore, for both these cases, the G_2^- parameter was reduced to 40 N/mm to promote a better fit between numerical and experimental load *vs.* CMCD curves; this change had the downside of introducing a higher relative difference in ultimate loads of -10% and -4%, for I150-AP and U150-ST, respectively (which were still deemed as acceptable).

Figure 13 (e) illustrates the impact of considering numerical tensile failure on I150-ST results. The discrepancy between tensile failure predictions in numerical and experimental results was addressed by considering the tensile cohesive stress (41 MPa) instead of the material strength (34 MPa) and by analysing the difference between the transverse tensile ($E_{22}^+ = 5.5$ GPa) and compressive ($E_{22}^- = 9.3$ GPa) elastic moduli. As the numerical models were developed considering the compressive elastic modulus, this may lead to a fictitious increase of tensile stresses in the posterior face of the specimens. This numerical issue was addressed through three different methods: (i) a model was developed with different and varying elastic moduli (tensile or compressive), as a function of the stress level in each element (positive or negative); (ii) in a more simplified approach, another model was sectioned to present different elastic moduli defined *a priori* in specific regions prone to compressive/tensile stresses; and (iii) finally, another model was developed with artificially increased transverse tensile strength, as a function of the elastic moduli ratio (E_{22}^-/E_{22}^+) and increased G_2^+, as a function of the squared elastic moduli ratio

$((E_{22}^-/E_{22}^+)^2)$. The first solution was achieved by adding a condition (if $\sigma_{22}>0$, then $E_{22}=E_{22}^+$) to the UMAT subroutine, whereas the second and third solutions were implemented through Abaqus built-in tools. These various solutions, which take into consideration the tensile cohesive stress and consider no residual stress, are illustrated in Figure 14 and compared to the initial numerical results ("Prelim.") presented in Figure 13 (e).

Figure 14 clearly shows that the first two solutions, which account for different elastic moduli in tension and compression, led to similar results; whereas increasing the tensile strength and fracture toughness led to an excessive increase of CMCD at brittle failure. In line with these results, the first solution, implemented in the UMAT, was considered to obtain the results described in the following sections.
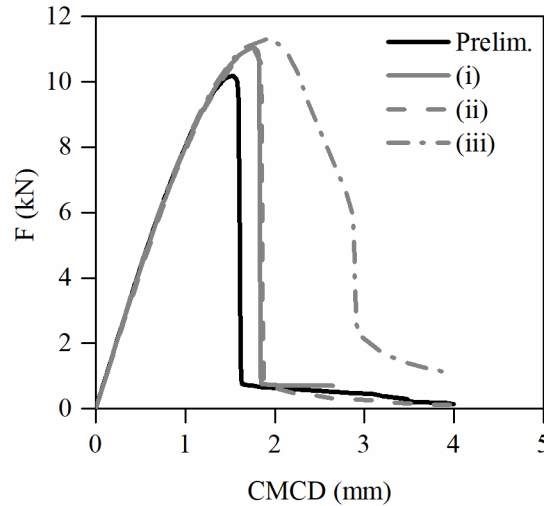

Figure 14: Numerical load *vs.* CMCD curves for I150-ST: (i) different and varying E_{22} as a function of σ_{22}; (ii) model sectioned to present compressive and tensile E_{22} in different regions defined *a priori*; (iii) model with increased σ_{22}^+ and G_2^+ properties as a function of the E_{22}^-/E_{22}^+ ratio.

4.2.3. Results from calibrated models

Figure 15 presents a summary of numerical and experimental load *vs.* CMCD curves, including the preliminary numerical results ("Prelim."), as well as the calibrated numerical results ("Calibrated"), as a function of the calibrations detailed in the previous section.

Figure 15 presents a good fit between numerical and experimental results, in terms of peak loads and failure modes. As a general trend, most numerical results showed a better fit to experimental results when calibrated with the cohesive stress (*vs.* the transverse tensile strength), including I150-AP results, despite being the only material where $\sigma_c<\sigma_{u22}^+$.

The experimental and numerical failure modes are compared in Figure 16, which illustrates specimens after failure and numerical plots of damage evolution for two distinct cases: (i) I152-CP, where damage developed exclusively due to compressive stresses; and (ii) I150-ST, where most specimens showed very little compressive damage propagation ($\approx$10 to 15 mm), before tensile damage led to failure. The numerical results are presented with respect to the shear damage parameter "DAMAGESHR" in Abaqus built-in tools and output variable "SDV14" in the user subroutine, which is an envelope for other damage parameters [21, 24]. This variable was chosen to highlight simultaneously tensile and compressive damage.
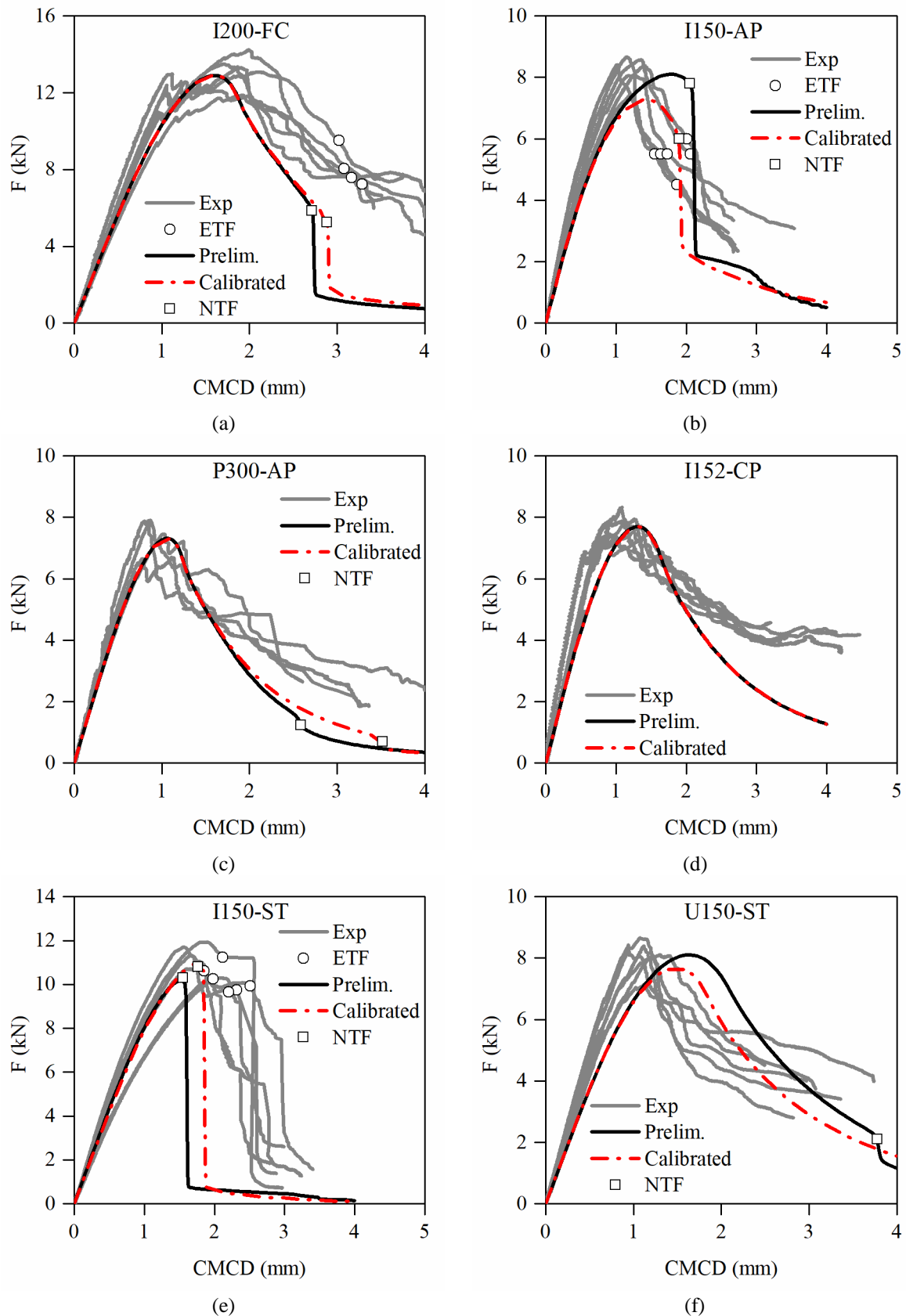
Figure 15: Load *vs.* CMCD curves of experimental tests, preliminary models ("Prelim.") and calibrated
("Calibrated") models: (a) I200-FC; (b) I150-AP; (c) P300-AP; (d) I152-CP; (e) I150-ST; (f) U150-ST.
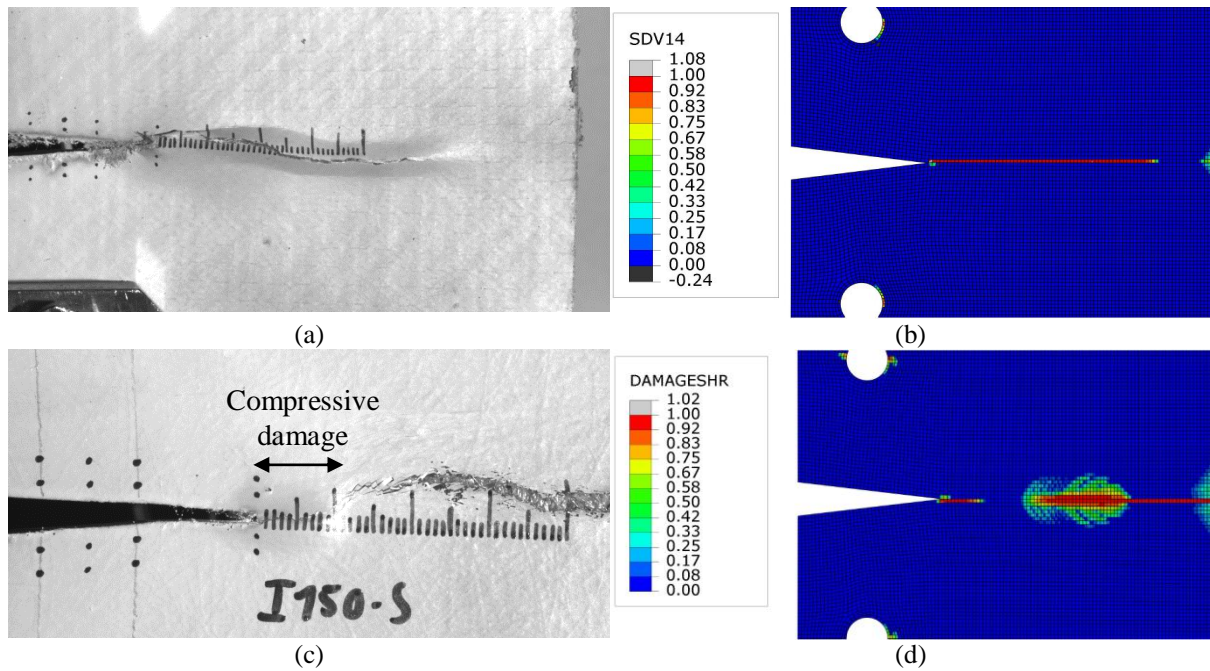
Figure 16: Experimental failure modes and numerical damage plots (shear damage parameter): (a) I152-CP-1; (b) I152-CP-Num (UMAT); (c) I150-ST-4; (d) I150-ST-Num (built-in tools).

4.3. Residual stress input calibration

Taking into account the models presented in the previous section, σ_r was finally calibrated to promote the best fit between numerical and experimental softening stages. Two materials were excluded from this analysis, I150-AP and I150-ST, as tensile failure affected the results early on, thus compromising the validity of the softening stage.

The residual stress analysis focused on the softening slope of these curves. To make this analysis more objective, the experimental curves were used to define an average softening curve. IBM SPSS [25] software was used to determine an exponential fitting law that produced the best fit to experimental curves. A three-parameter function was used for these calibrations, as follows,

$$F = a.e^{-b.CMCD} + c \qquad (4)$$

where "a", "b" and "c" are fitting parameters.

Figure 17 presents numerical and averaged experimental load *vs*. CMCD softening curves, considering different values of σ_r, defined as a fraction of σ_{u22}^-. To this end, the experimental load *vs*. CMCD curves were processed to produce an averaged softening curve, thus enabling a comparison between numerical and experimental results. Furthermore, peak load discrepancies were discarded (which are mainly affected by G_2^-, but not by σ_r) as well as stages where tensile damage had initiated. To that end, the load *vs*. CMCD curves presented in Figure 17 correspond to the variation of CMCD after the peak load is attained, for a load/ultimate load ratio lower than ≈95%. Therefore, with this procedure, all discrepancies between experimental and numerical results should be solely attributed to the softening slopes.
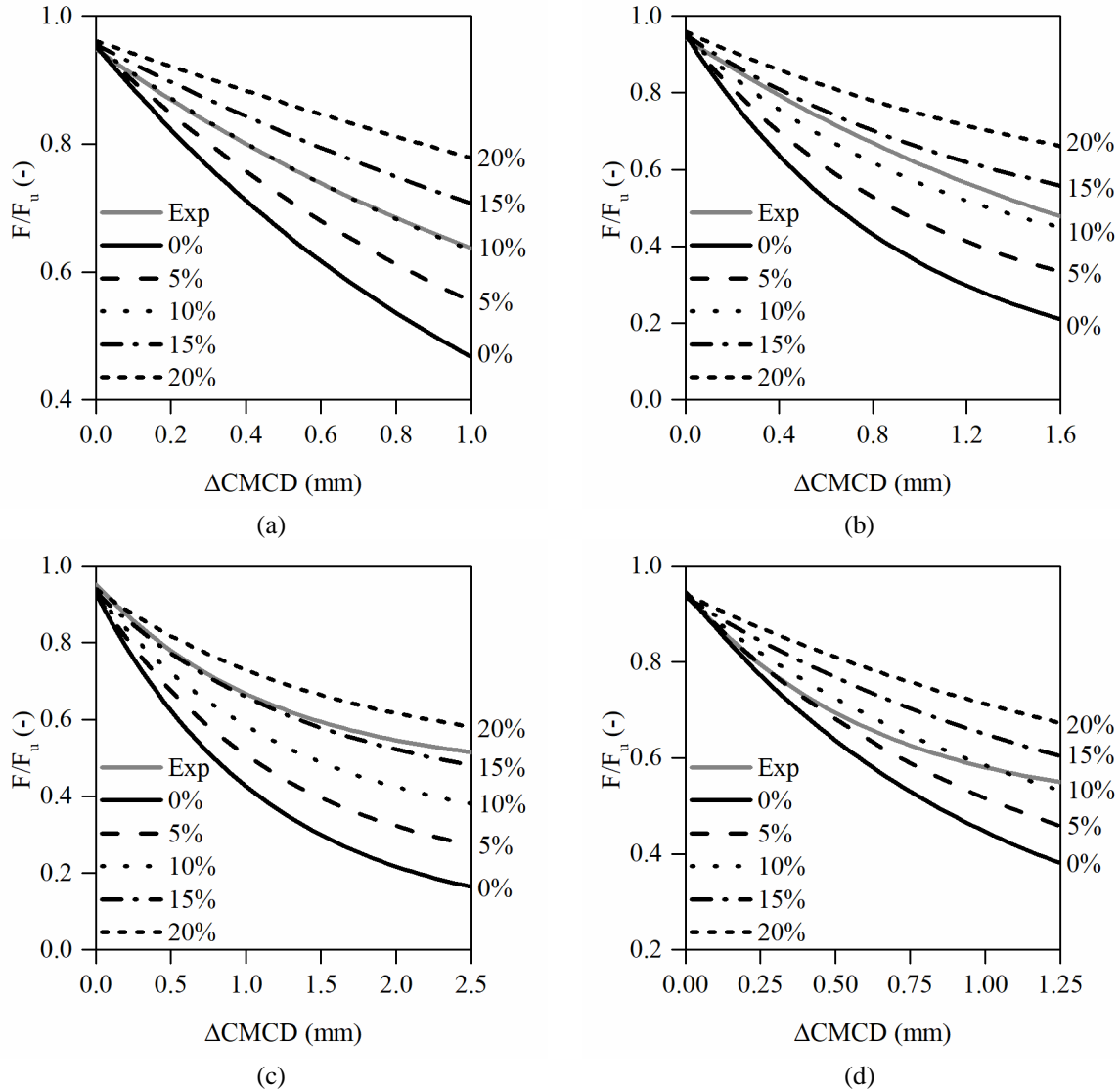
Figure 17: Experimental and numerical load *vs.* CMCD softening stages, for different σ_r/σ_{u22}^- ratios (%): (a) I200-FC; (b) P300-AP; (c) I152-CP; (d) U150-ST.

The results shown in Figure 17 illustrate the significant impact of σ_r on the softening stage, as expected. It is noteworthy that adequate results were obtained for all materials for a range of σ_r between 5% and 20% of σ_{u22}^-. It is also noticeable that the models for U150-ST were unable to fully capture the experimental softening trend, unlike the models for the remaining GFRP materials. At this time, this is attributed to a potential overestimation of G_2^-, which led to similar ultimate load results, but also to a significantly smoother numerical softening slope near the peak load.

In order to have an objective measure of the fitting of numerical and experimental curves, the numerical softening curves were also fitted with exponential functions as described in (4). Then, the absolute difference between numerical and experimental curves could be determined. This process led to the results summarized in Figure 18.

Figure 18 highlights a narrow range between 9% and 16% for the optimal ratios between σ_r and σ_{u22}^- of the four materials analysed, which corresponds to an absolute range between 7.6 MPa (U150-ST) to 16.9 MPa (P300-AP). From these results, it may be concluded that material properties and fibre layups have low influence on the transverse compressive residual stress; it is possible that such parameter depends mainly on the polymeric matrix. In a different trend, the thinnest materials are those that present higher σ_r values (12.5% and 16%, for P300-AP and I152-CP, respectively). These results may be related to the fact that thinner materials are typically more resistant to delamination phenomena, which occurred in parallel with compressive damage propagation. Future developments should further assess these

trends, so that the residual stress of a given GFRP material can be further established and linked to its geometry, material properties, fibre layup and type of polymer matrix.
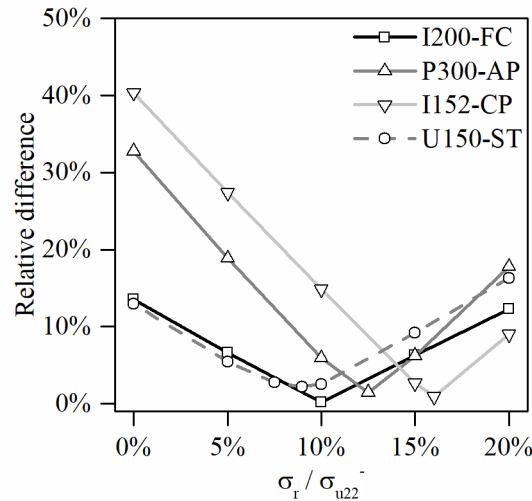

Figure 18: Averaged relative difference between numerical and experimental softening curves.

5. Comparison between G_2^- and G_2^+

This section presents a brief discussion about the ratio between compressive and tensile fracture properties, also taking into account the transverse reinforcement percentages of each material. Figure 19 illustrates the evolution of compressive and tensile [14, 15] values of fracture toughness with the transverse reinforcement percentage, including fitting functions of these results (FF). It should be taken into consideration that the different resins used for the various materials should influence the compressive results more significantly than the tensile results, which depend foremost of the fibre structure. Despite using only polyester based materials, the exact resin compositions are unknown, and thus the analysis has been kept to the transverse reinforcement percentages and fibre layups, as presented in Table 1 and further detailed in [15].

Figure 19 (a) shows different trends between compressive and tensile fracture properties. Unlike G_2^+, which has an increasing trend with the transverse reinforcement, G_2^- presents the highest value for a material with very low transverse reinforcement, solely provided by CFM layers. The other materials present results in a narrow range (36 to 48 N/mm), with an average of 41 N/mm. Aside from one case (I152-CP), all materials presented significantly higher transverse compressive fracture toughness, when compared to the transverse tensile fracture toughness.

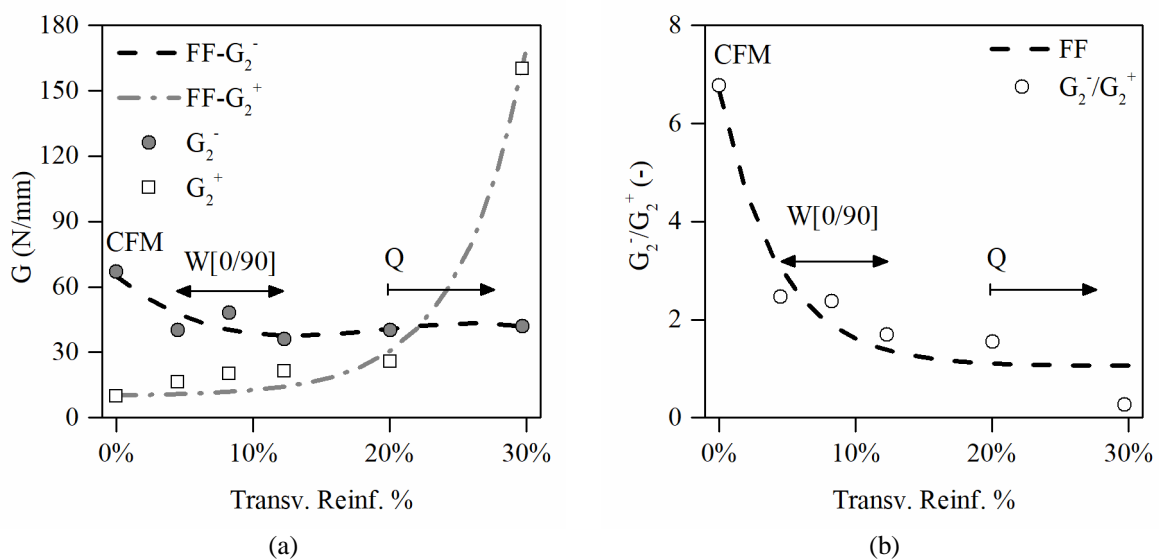
(a)   (b)

Figure 19: Evolution of fracture toughness results for tension [15] and compression as a function of transverse reinforcement percentages [15]: (a) absolute values; (b) G_2^-/G_2^+ ratio.

The ratio between transverse compressive fracture toughness and tensile fracture toughness, illustrated in Figure 19 (b), presents a clear decreasing trend as a function of the transverse reinforcement percentage. These results must be further validated, namely with other FRP materials with similar fibre layups, in order to assess the validity of this trend. It will also be important to compare similar layups with different polymeric resins, in order to better understand the contribution of the resin to the transverse compressive fracture behaviour of FRP materials.

6. Conclusions

This paper presented a study about the transverse fracture behaviour of pultruded glass fibre reinforced polymer (GFRP) in compression, with focus on the assessment of transverse compressive fracture toughness (G_2^-) and transverse compressive residual strength (σ_r). These properties were assessed through experimental Compact Compression tests. In face of experimental overestimations of fracture toughness, obtained through standard data reduction schemes, a numerical study was conducted to determine these properties by fitting numerical and experimental load *vs*. CMCD curves. The calibration process considered two main parameters, G_2^- and σ_r, which represents the crushing of the material in the damaged area. The G_2^- values varied between 36 and 67 N/mm and the optimal σ_r values ranged from 9% to 16% of the transverse compressive strength (absolute values ranged from 7.6 to 16.9 MPa).

The numerical results showed that thinner materials have slightly higher σ_r/σ_{22u}^- ratios (12.5% and 16%, for P300-AP and I152-CP, respectively), when compared to thicker materials (10% and 9%, for I200-FC and U150-ST, respectively), which may be due to the higher proneness to delamination of the latter. The numerical models were also validated by comparing numerical and experimental failure modes. This procedure involved additional calibration of tensile properties because several specimens presented a failure mode triggered by tensile damage at their posterior face, after compressive damage had initiated. It is noteworthy that most numerical models presented a better agreement to experimental tests when the cohesive stress, previously measured through tensile fracture tests, was considered instead of the mechanically characterized transverse tensile strength. The results also showed a significantly different variation of G_2^- with the transverse reinforcement percentage (45° and 90° oriented layers), when compared to previous results for G_2^+. The G_2^-/G_2^+ ratio was found to drop significantly with the transverse reinforcement percentage, highlighting the possible influence of the polymeric resins used in each material.

The assessment of the fracture behaviour of GFRP materials produced with similar fibre layups but different polymeric resins should be considered as a relevant future development. Finally, as this experimental campaign focused on a single test configuration, it will also be important to confirm the presented compressive fracture properties for a wider range of geometries and test configurations.

Acknowledgements

References

[1] Maimí, P., Camanho, P. P., Mayugo, J. A., & Dávila, C. G., A continuum damage model for composite laminates: Part II - Computational implementation and validation. *Mechanics of Materials*, 39(10), 909–919, 2007.

[2] Ratcliffe, J., Jackson, W., & Schaff, J., Predicting the compression strength of impact-damaged sandwich panels. *American Helicopter Society 60th Annual Forum*, Baltimore, 2004.

[3] Pinho, S. T., Robinson, P., & Iannucci, L., Fracture toughness of the tensile and compressive fibre failure modes in laminated composites. *Composites Science and Technology*, 66(13), 2069–2079, 2006.

[4] Pinho, S. T., Gutkin, R., Pimenta, S., De Carvalho, N. V., & Robinson, P., On longitudinal compressive failure of carbon-fibre-reinforced polymer: from unidirectional to woven, and from virgin to recycled. *Phil. Trans. R. Soc. A, Physical and Engineering Sciences*, 370, 1871–1895, 2012.

[5] Laffan, M. J., Pinho, S. T., Robinson, P., & Mcmillan, A. J., Translaminar fracture toughness testing of composites: A review. *Polymer Testing*, 31(3), 481–489, 2012.

[6] Martins, D., Proença, M., Correia, J. R., Gonilha, J., Arruda, M., & Silvestre, N., Development of a novel beam-to-column connection system for pultruded GFRP tubular profiles. *Composite Structures*, 171, 263–276, 2017.

[7] Almeida-Fernandes, L., Gonilha, J., Correia, J. R., Silvestre, N., & Nunes, F., Web-crippling of GFRP pultruded profiles. Part 1: Experimental study. *Composite Structures*, 120, 565–577, 2015.

[8] Almeida-Fernandes, L., Nunes, F., Silvestre, N., Correia, J. R., & Gonilha, J., Web-crippling of GFRP pultruded profiles. Part 2: Numerical analysis and design. *Composite Structures*, 120, 578–590, 2015.

[9] Nunes F., Silvestre N., Correia J. R. "Progressive damage analysis of web crippling of GFRP pultruded I-sections", *Journal of Composites for Construction*, 21(3), 1–13, 2016.

[10] Laffan, M. J., Pinho, S. T., Robinson, P., & Iannucci, L., Measurement of the in situ ply fracture toughness associated with mode I fibre tensile failure in FRP. Part I: Data reduction. *Composites Science and Technology*, 70(4), 606–613, 2010.

[11] Laffan, M. J., Pinho, S. T., Robinson, P., & Iannucci, L., Measurement of the in situ ply fracture toughness associated with mode I fibre tensile failure in FRP. Part II: Size and lay-up effects. *Composites Science and Technology*, 70(4), 614–621, 2010.

[12] El-Hajjar, R., & Haj-Ali, R., Mode-I fracture toughness testing of thick section FRP composites using the ESE(T) specimen. *Engineering Fracture Mechanics*, 72(4), 631–643, 2005.

[13] Liu, W., Feng, P., & Huang, J., Bilinear softening model and double K fracture criterion for quasi-brittle fracture of pultruded FRP composites. *Composite Structures*, 160, 1119–1125, 2016.

[14] Almeida-Fernandes, L., Silvestre, N., Correia, J. R., Characterization of transverse fracture properties of pultruded GFRP material in tension, *Composites Part B: Engineering*, 175, 107095, 2019.

[15] Almeida-Fernandes, L., Correia, J. R., Silvestre, N., Transverse fracture behaviour of pultruded GFRP materials in tension: Effect of fibre layup, *Journal of Composites for Construction*, in press.

[16] Ortega, A., Maimí, P., González, E. V., & Trias, D., Characterization of the translaminar fracture Cohesive Law. *Composites Part A: Applied Science and Manufacturing*, 91, 501–509, 2016.

[17] Ortega, A., Maimí, P., Gonz, E. V, Sainz de Aja, J. R., de la Escalera, F. M., & Cruz, P., Translaminar fracture toughness of interply hybrid laminates under tensile and compressive loads. *Composites Science and Technology*, 143, 1–12, 2017.

[18] Zobeiry, N., Vaziri, R., & Poursartip, A., Characterization of strain-softening behavior and failure mechanisms of composites under tension and compression. *Composites Part A: Applied Science and Manufacturing*, 68, 29–41, 2015.

[19] Simulia, "Abaqus/CAE 2018", 2018.

[20] ASTM D6641 / D6641M – 09, *Standard Test Method for Compressive Properties of Polymer Matrix Composite Materials Using a Combined Loading Compression (CLC) Test Fixture*, ASTM International, West Conshohocken, Pennsylvania, 2009.

[21] Almeida-Fernandes, L., Silvestre, N., Correia, J. R., Arruda, M. R. T., Fracture toughness-based models for damage simulation of pultruded GFRP materials. *Composites Part B: Engineering*, 186, 107818, 2020.

[22] Lopes, B., Arruda, M.R.T., Almeida-Fernandes, L., Castro, L., Correia, J.R., *Mesh Dependency Tests for Orthotropic Continuum Damage Model*, CERIS Report, November, 33, 2019.

[23] Girão Coelho, A. M., Toby Mottram, J., & Harries, K. A., Finite element guidelines for simulation of fibre-tension dominated failures in composite materials validated by case studies. *Composite Structures*, 126, 299–313, 2015.

[24] Hashin, Z., and Rotem, A., A fatigue criterion for fiber-reinforced materials, *Journal of Composite Materials*, 7, 448-464, 1973.

[25] IBM, "SPSS statistics", 2016, version 24.